Chapter 11
Micro/Nanorobotic Manufacturing of Thin-Film NEMS Force Sensor

Gilgueng Hwang and Hideki Hashimoto

Abstract This chapter presents the fabrication and characterization of piezoresistive force sensors based on helical nanobelts. The three-dimensional helical nanobelts are self-formed from 27-nm-thick n-type InGaAs/GaAs bilayers using rolled-up techniques and assembled onto electrodes on a micropipette using nanorobotic manipulation. Patterned gold electrodes were fabricated using thermal evaporation or fountain-pen-based gold nanoink deposition. Nanomanipulation inside a scanning electron microscope was conducted to locate small metal pads of helical nanobelts to be connected to the fabricated pipette-type electrodes. Gold nanoink was deposited under optical micrograph using the fountain-pen method. Nanomanipulation inside a scanning electron microscope using a calibrated atomic force microscope cantilever was conducted to calibrate the assembled force sensors, and the values were compared with finite-element-method simulation results. With their strong piezoresistive response, low stiffness, large-displacement capability, and good fatigue resistance, these force sensors are well suited to function as sensing elements for high-resolution and large-range electromechanical sensors.

11.1 Introduction

In recent decades, various micro-/nanoelectromechanical systems (MEMS/NEMS) have been used for many applications. Much effort has been devoted to the innovative process of synthesizing micro-/nanostructures as the building blocks

G. Hwang (✉)
Laboratory for Photonics and Nanostructures, Centre National de la Recherche Scientifique, Marcoussis 91460, France
e-mail: gilgueng.hwang@lpn.cnrs.fr

H. Hashimoto
Department of EECE, Chuo University 1-13-27 Kasuga, Bunkyo-ku, Tokyo, Japan

M. Rakotondrabe (ed.), *Smart Materials-Based Actuators at the Micro/Nano-Scale: Characterization, Control, and Applications*, DOI 10.1007/978-1-4614-6684-0_11,
© Springer Science+Business Media New York 2013

for creating such MEMS or NEMS [1, 2]. Carbon nanotubes (CNTs) [3–6], nanowires (NWs) [7], and Nanohelixes [8–13] are the most widely synthesized and considered the promising elements in NEMS and nanoelectronics. For their successful applications, the packaging process to construct devices from these new building blocks and the characterization of the devices are among the most critical steps to proving their quality for working in application environments. For example, with field emitting displays, the major packaging challenge is to achieve directionally controlled growing of NWs and CNTs. For this purpose, the mechanical properties of these nanostructures should be understood precisely. Electrical property characterizations is another practical issue along with device packaging. Regarding packaging, a bottom-up approach like self-assembly is the most widely used. A top-down approach using micro-/nanolithography and etching processes is another process. In addition to the top-down approach, micro-/nanoassembly could be an alternative approach to creating devices or prototypes [14–16]. This approach is based on micro-/nanorobotic manipulation systems with precise MEMS/NEMS sensors and actuators installed inside nanoscale imaging devices such as scanning/transmission electron microscopes (SEM/TEM). In particular, wide-range mechanical pressure/force sensors are among the most important devices that should be integrated into robotic manipulations to characterize the mechanical/electrical and even electromechanical properties of various nanostructures. The characterized physical properties are essential to establish a precise model of nanostructures. Physical models of single nanostructures are essential for the device engineering and performance optimization of the NEMS sensors/actuators constructed from them. Force sensing is the most widely used tool to characterize the mechanical properties of these structures.

In this chapter, we demonstrate the micro-/nanorobotic manufacture of thin-film NEMS force sensors to have a large force-sensing range. For example, force sensing probes based on the piezoresistivity of InGaAs/GaAs helical nanobelts (HNBs) is introduced. HNBs can serve as a mechanism to transduce force to displacement. The deformation is detected through a piezoresistive effect to measure the corresponding force after calibration. A major challenge in the development of the proposed force sensor is the lack of manufacturing processes. Therefore, this chapter describes the details of the micro-/nanorobotic manufacturing process of such three-dimensional thin-film nanodevices.

11.2 Helical Nanobelt Force Sensors

11.2.1 Large-Range Force Sensors

Force sensing with high enough precision but large bandwidth is essential to in particular small-scale robotics applications (mechanical characterizations of nanostructures, robotic drug delivery, single-molecule detection from a whole bunch of molecules, robotic injection, etc.) [17, 18]. Kinking and buckling force mea-

Table 11.1 Required specification of force sensor in nanomanipulation

Dimension	∼a few tens of microns
Force-sensing range	nN ∼ a few hundred nanonewtons
Displacement range	1 nm to a few microns
Force-sensing direction	Arbitrary direction
Force-sensing mechanism	Self-sensing mechanism

surements are shown to be very important in the understanding of the mechanical properties of newly synthesized nanomaterials for determining their competitive NEMS applications [19, 20]. To fulfill these nanomanipulation tasks, it is highly expected that NEMS-based force sensors will be developed.

The required features of force sensors to fulfill these tasks are summarized in Table 11.1. These requirements were based on empirically obtained knowledge from nanomanipulations of nanostuctures such as CNTs, NWs, etc. They were also obtained from published works on nanomanipulations [19, 20]. Meanwhile, an increasing number of applications in nanorobotic manipulations require an nanonewton range force sensing [21]. Conventionally, mechanical transducers have been developed. A scanning force microscopy (SFM) cantilever is used mostly for sensing forces in a range of 10 pN–100 nN [22]. Microneedles have been used to measure the force of a single actin filament [23]. Photon-field-based optical tweezers [24] have been used for force sensing in a range of 0.1–100 pN [22]. This laser-based sensing can heat biological samples, and so its application is limited. A magnetic field can measure below 10 pN by manipulating an attached magnetic bead [25]. However, it has also a drawback in that it requires indirect measurement of the magnetic force. Flow fields in a laminar flow can measure 0.1 pN–1 nN [22]. To reach this sensing resolution in a more systematic way, many NEMS force-sensing devices have been demonstrated in several different types such as in-plane devices and out-of-plane probes. As an in-plane force and pressure sensor, an individual single-walled carbon nanotube (SWNT) was bridged between two electrodes using the characterized piezoresistivity [26, 27]. For out-of-plane device transduction, CNTs were attached to an atomic force microscope (AFM) cantilever [3–5]. However, there are still no built-in sensing elements have been demonstrated for such cantilevers due to their nanometer sizes, whereas similar MEMS force sensors, such as piezoresistive cantilevers [28, 29] and capacitance sensors [30], have been fabricated. On the other hand, three-dimensional (3D) helical structures with micro- and nanofeatures have been synthesized from various materials. Typical examples include microcoils based on amorphous carbon [8], nanocoils based on CNTs [9], and zinc oxide HNBs [10, 11]. Because of their interesting morphology, as well as mechanical [12, 13], electrical, and electromagnetic properties, these micro-/nanostructures can be used as components for MEMS and NEMS such as springs, inductors, sensors, and actuators. Recently, the electrical and mechanical properties of SiGe/Si/Cr and SiGe/Si HNBs were characterized separately through experiments and simulations [12]. The fabrication and mechanical characterization of InGaAs/GaAs HNBs have been also described [13]. Their excellent flexibility provides a new avenue for fabricating ultra small force sensors with high resolution.

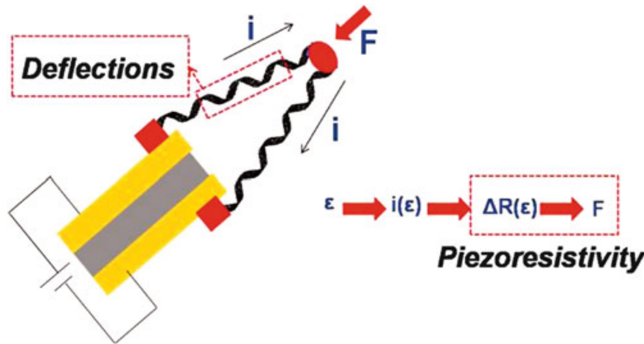

Fig. 11.1 Schematic of working principle of HNB force sensors

11.2.2 Piezoresistive Helical Nanobelt Force Sensors

The helical morphology benefits the ultraflexible mechanical property compared to beam-type cantilevers. Therefore, helical nanostructures such as HNBs have a large displacement range and high resolution. By determining the piezoresistivity in HNBs, arbitrary directional force sensing and easy integration with nanomanipulators from self-sensing are achievable. Therefore, our approach is to build a force sensor with an ultraflexible structure from a helical morphology. As a sensing mechanism, the piezoresistivity of InGaAs/GaAs HNBs for force sensing is characterized first. Since the proposed design undergoes both axial and bending forces, the corresponding piezoresistivities in multiple axes were also characterized to estimate the piezoresistivity effect after the force sensor assembly. Nanorobotic assembly processes were proposed mainly for the field-assisted alignment of HNBs onto a pipette electrode and for electrical soldering to assure an ohmic conductivity. The assembled HNB force sensor was characterized using an as-calibrated AFM cantilever. The force sensor was able to measure the applied force by reading the resistance change from the HNBs' piezoresistivity. HNBs represent a new material and are much more flexible and fit our out-of-plane devices. HNBs have very nice features: for example, they are ultrasoft and uniform in geometry and have easy band-gap tuning. Their drawbacks include mainly that they have a high surface-to-volume ratio, making soldering difficult, and their ultra flexibility with an ultra-thin film can lead to misalignment or uncontrolled assembly. Most of the assembly technologies that have been investigated so far do not work well with 3D HNBs. To solve these problems, we have proposed better alignment technologies of HNBs using an external field assist. Furthermore, we propose robust soldering technologies which can be applied to various scales (gold nanoink deposition, in situ extension of gold nanoink soldering, and chemical-free resistance spot welding) for 3D structures.

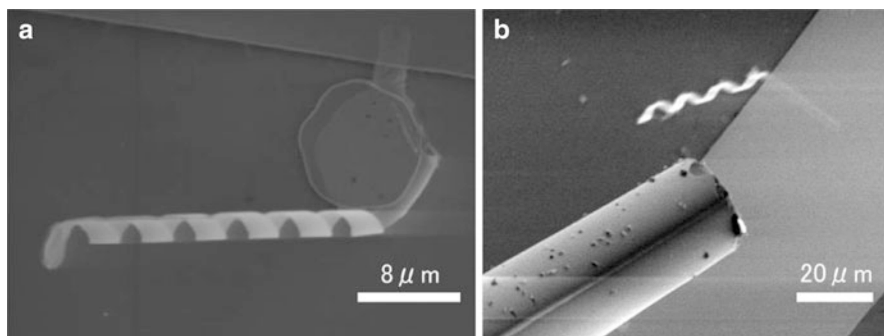

Fig. 11.2 As-fabricated (**a**) InGaAs/GaAs HNBs with metal pads and (**b**) electrodes on tapered micropipettes

11.2.3 Working Principle of HNB Force Sensors

As shown in Fig. 11.1, HNB force sensors measure the force by piezoresistivity. When a certain amount of force is applied to a HNB force sensor, the deflection of the HNB changes the resistance of the assembled structure. Figure 11.1 shows a schematic view of the proposed HNB force sensors. Two HNBs with metal connectors are assembled on an independently patterned micropipette electrode. Then each electrode passing through two HNBs is interfaced outside to determine the strain (ε)-induced current change given a constant voltage input.

11.3 Force Sensor Assembly

11.3.1 Interconnection Layer Fabrication

NEMS using HNBs include two typical configurations [31], i.e., a HNB bridging two electrodes horizontally or standing vertically on electrodes. An as-fabricated HNB is shown in Fig. 11.2. To obtain a better interconnection conductivity, HNBs were fabricated with metal connectors (Cr/Ni/Au 20/200/25 nm) on both ends [32], which is different from the standard design [31]. Microtapered pipette-type electrodes were prepared [33]. A ferromagnetic Ni layer was evaporated at the end of the HNB for electromagnetic actuation. Figure 11.2 shows the as-fabricated pipette electrodes used to assemble HNBs. The electrode pattern was generated by thin-film evaporation. Our objective is to assemble suspended HNBs on the as-fabricated pipette electrodes (Fig. 11.2b), Cr/Ni/Au deposited independent electrodes, for precise location of HNBs with metal deposited connectors. First, the borosilicate capillary was pulled to make tapered micropipettes. The dimensions of the pipette opening were controlled in a reproducible way using a micropipette puller (DMZ Universal Puller, Zeitz Instruments, Germany). Pipettes with 1 and

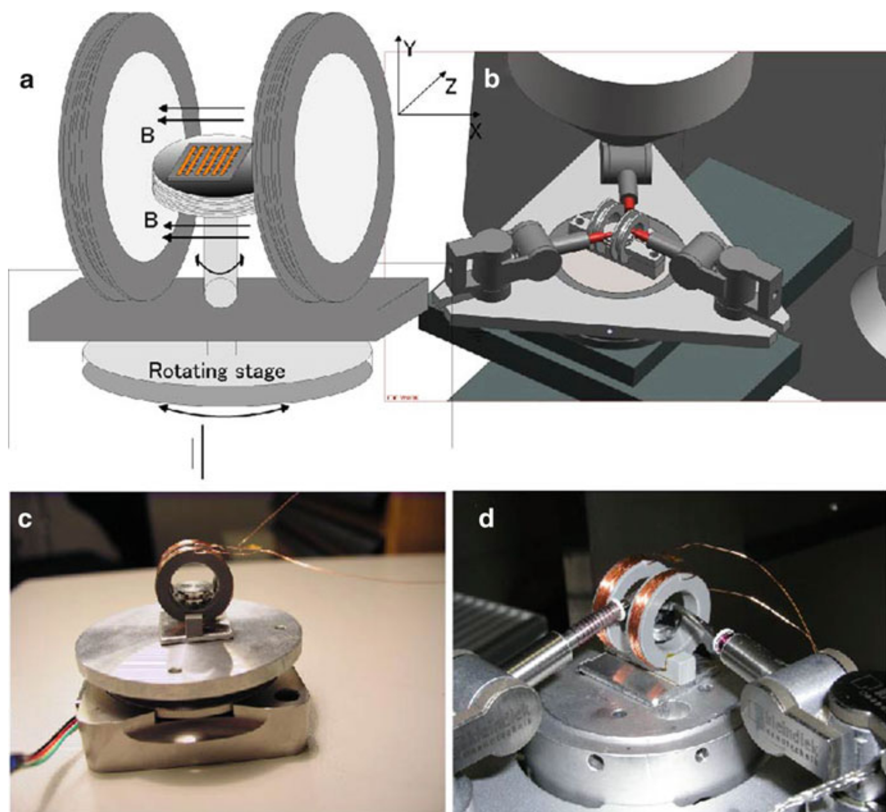

Fig. 11.3 Experimental setup: (**a**) Helmholtz coil on piezoelectric rotational stage, (**b**) CAD model of integration with manipulators, (**c**), (**d**) manipulators and Helmholtz coil installed inside SEM

15 μm openings were fabricated. Then, independent Cr/Ni/Au metal layers were evaporated on both sides of the pipette by changing the exposure to the target electron-beam-heated metal source. A homemade pipette holder with wiring was used to mount to a nanomanipulator and connect to the power supply.

11.3.2 External Force-Generating System

The nanorobotic manipulation system shown in Fig. 11.3 was used for the manipulation of the as-fabricated HNBs inside a SEM (Carl Zeiss DSM 962). Three nanorobotic manipulators (Kleindiek, MM3A) were installed inside the SEM; each had three degrees of freedom and 5-, 3.5-, and 0.25-nm resolution in the X-, Y-, and Z-directions at the tip. A metal probe (Picoprobe, T-4-10-1 mm, tip radius: 100 nm) was mounted on the nanomanipulator. The same manipulation setup was used for both the assembly and the characterizations.

Table 11.2 Experiment specifications

Gap r [µm]	5
Length [µm]	36.3
R_{ext} [µm]	1.05
R_{int} [µm]	1.023
Electric constant e_0 [C^2/Nm^2]	$8.85 \cdot 10^{-12}$
Voltage range V [V]	0-1;Step:0.1 V
E-module [N/m^2]	$8.0215 \cdot 10^{10}$

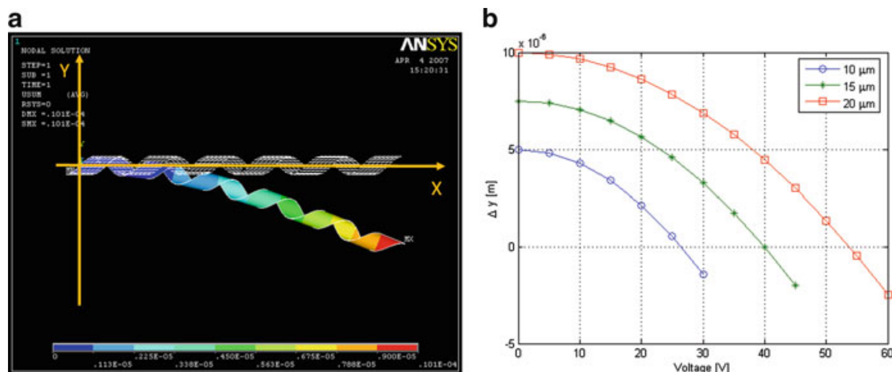

Fig. 11.4 FEM simulation of HNB by ANSYS. (**a**) Bending force simulation for closing HNBs; (**b**) voltage as a function of HNB deflection for different gaps (10, 15, and 20 µm)

Additionally, we designed a Helmholtz coil to generate the required external magnetic force to assemble the HNB (Fig. 11.3). For use inside the SEM chamber, we should consider the working distance of an electron beam and sample stage. Rings 21 mm in diameter were used to wind coils, and these coils were grounded onto the sample stage to prevent charging from the electron beam.

A single SEM sample holder was located between two coils. Samples were placed onto the sample holder between two coils. With this coil configuration, we measured a 2-mT magnetic field at 2.3 V, 0.254 A, which was required to deflect the magnetic pads on both ends of the HNB. A sample holder was also coiled so as to have a vertical axis magnetic field that achieved 1.3 mT at 2 V, 0.554 A. This coil was mounted onto a piezoactuated rotating nanostage, as shown in Fig. 11.3. Two nanomanipulators were installed through the coils to work over the sample chip. We experienced SEM imaging distortion over 5.5 V, which caused heating and melted the plastic part of coils.

11.3.3 External Field-Assisted Assembly

Finite-element-method (FEM) simulation was used to estimate the applied force on the HNBs in the experiments. The dimensions of the HNBs used in the simulation were the same as in the experiments, as summarized in Table 11.3. The simulation

Table 11.3 Specifications of HNBs used for simulation

Length [μm]	36.3
Radius [μm]	1.05
Pitch [μm]	6.6
Width [μm]	3
♯ of turns	5.5
Stiffness [N/m]	0.0001
Force [pN]	0.001–1

result was previously validated with experimental results for similar structures [13]. Simulation was carried out in an linear elastic range (small displacements). The values of the material properties in the model were taken from [13] with the rule of mixture applied for the InGaAs layer. Both ends of the helix were constrained from rotation around all three axes. Moreover, on one end of the helix was constrained from all translational movements, and on the other end it was constrained from translational movement perpendicular to the axis. On this end, a force in the axial (X-axis) or bending (Y-axis) direction was applied to compute the displacement.

In Fig. 11.4, a plot of the displacement along the bending direction is shown. From the simulation, the bending stiffness of the structure was determined to be 0.0001 N/m, as summarized in Table 11.3. The first thing to do was the preparation of the sample and the installation of the manipulators. In fact, if the pipette were touched with bare hands, without protection, the electrostatic discharge (ESD) could have broken the thin part of the pipette. For this reason, a bracelet and special gloves were used to ground it during the installation.

In Fig. 11.5, we see that the probe is in contact with and forms an electric circuit with the suspended HNB. The HNB plays the role of a switch. In Fig. 11.5c, the circuit is closed, whereas in Fig. 11.5d it is open. The pipette had to be as close as possible to the HNB until it touched the HNB (the circuit was closed). At this point, an SEM image was grabbed for the initial state. Then the pipette was moved from its present position on the y-axis until the contact between the pipette and the HNB was broken and another new image was grabbed. In the end two images (Fig. 11.5) were compared to determine the extent to which the HNB was deflected (Δd). This procedure was repeated with different voltages. When all the results were analyzed (voltage or current versus Δd), we finally obtained the curve shown in Fig. 11.6a. It shows the linear relation between the voltage and the deflection, except for the drop at 8 V, which was caused by an unequal contact configuration.

The next experiment to be discussed is similar to previous tests. This time, however, we used Helmholtz coils to generate a uniform EM field (Fig. 11.5). Between the coils, a sample with HNBs was mounted. The experiment consisted in moving the pipette until it was in contact with the HNB. This was the initial state; then the pipette was moved from this position until the pipette–HNB contact was released. As was described in the previous experiment, images at each time were grabbed for the deflection measurement.

Fig. 11.5 Experiment: deflection of HNB by EM force (**a**), (**b**), deflection of HNB by ES force (**c**), (**d**)

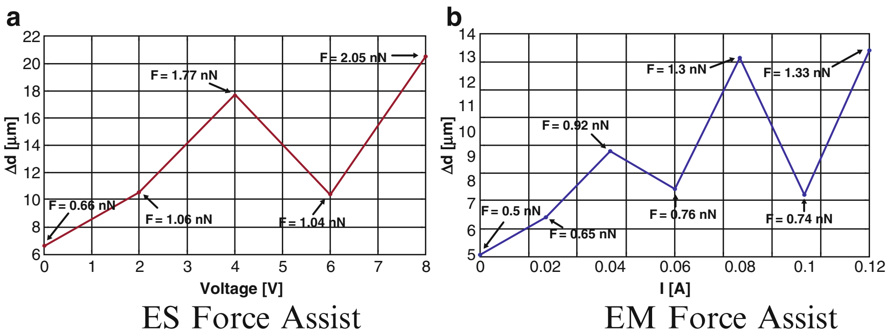

Fig. 11.6 Experiments with ES force (**a**) and EM force assistance (**b**): deflection [μm]

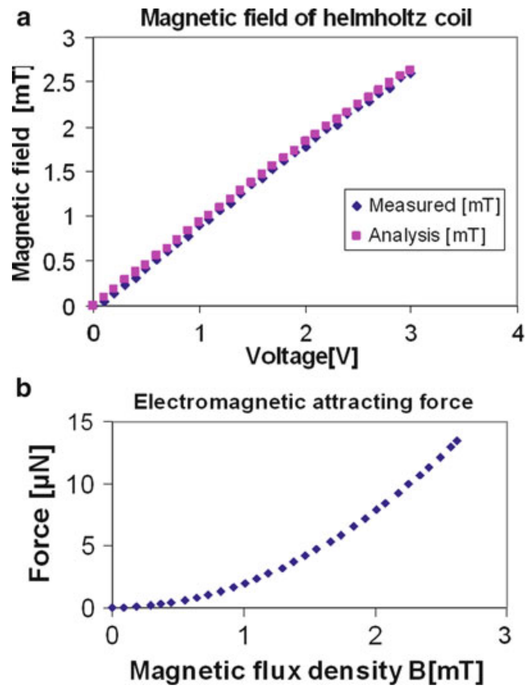

Fig. 11.7 Electromechanical characterization of magnetic HNB. (**a**) magnetic field measurement of Helmholtz coil. (**b**) Magnetic attracting force between probe and Ni pad

Figure 11.6b plots deflection versus the current flowing through the Helmholtz coil. It should be noted that there is a limit on the current, and a current that exceeds the limit results in SEM image distortion. In fact, the curve of the plot increases linearly. It was improved by several attempts with an ESD. A few problems remain with respect to decoupling the EM force itself from ES or van der Waals forces. However, the current result is sufficient to show that the EM field contributed the magnetization of the metal pads of the HNBs.

Given the coil setup, we measured a 2-mT magnetic field at 2.3 V, 0.254 A. Then the resistance was calculated using Ohm's law with $R = 2.3[\mathrm{V}]/0.254\,[\mathrm{A}] = 9.055\ [\Omega]$. In Fig. 11.6b, we use the current $I = 0.12\,[\mathrm{A}]$ to measure the voltage: $V = R/I = 1.086\,[\mathrm{V}]$. For a voltage of 1.086 [V] we obtained a B-field of 0.9 [mT] from Fig. 11.7a. We obtained an attracting force between the probe and Ni pad of 0.2 [μN] from a magnetic field of 0.9 [mT]. Then we were able to compare the estimated force with the experimental result in Fig. 11.6b. It showed a force of 1.33 [nN] for a current of $I = 0.12\,[\mathrm{A}]$. This very large difference can be explained by the fact that the analytical result was an ideal case with surface-to-surface contact between metal pad and pipette. However, as shown in Fig. 11.5, we could only on the side of the pad, which reduced the adhesive force. We also needed to consider that the HNB was fixed on one side; this means that the torsion force played a bigger role.

$$q_{\text{elec}} = \frac{\pi \varepsilon_0 V^2}{R\sqrt{\frac{r(r+2R)}{R^2}}\log^2(1+\frac{r}{R}+\sqrt{r(r+2R)}R^2)} \tag{11.1}$$

In theory, we have explained the equation of the ES force (11.1), and along with that we have conducted a few simulations to understand the behavior of the voltage as a function of the deflection. A MATLAB script to calculate the force with different HNBs was prepared, which was useful for the iterative simulations. We used different gaps between HNBs. The gap distances were set at 10, 15, and 20 µm. It should be noted that the pull-in voltage or the voltage necessary to collapse HNB to the electrode was found in the middle of the gap. This means that two HNBs were attached together at this position. In (11.1), we must insert the gap (r), the voltage (V), and the radius of the HNB turn (R_{ext}) (Table 11.2).

The calculated force using the MATLAB script was used in another MATLAB script to create a HNB model for simulation in ANSYS. We had to change step by step the force data in the file and compile and start in ANSYS the simulation in accordance with the determined deflection. Finally, we were able to obtain the relation between the voltage and the deflection of the HNBs. The results of this simulation are shown in Fig. 11.4b. The pull-in voltage of 27 V was obtained in the case of a 10-µm gap. We should not consider the result with a negative value in the graph because the two HNBs, when the distance 0 µm was reached, were attached together, so the HNBs were not able to exceed this distance. We had these negative data from the ANSYS simulation because we had used a range of voltages (for the force) without considering the limit. In the second case (15-µm gap), the voltage was 40 V, and in the third (20-µm gap) it was 54 V. An entire assembly procedure inside the SEM with the assistance of an external field was conducted and is introduced at the end of this section. A piezoresistive HNB force-sensing probe was assembled using the proposed method. It was conducted by serial nanorobotic assembly with an external electrostatic and electromagnetic force assist. The force-sensing probe showed piezoresistivity by deflection and was calibrated with an as-calibrated atomic force microscope cantilever.

The HNB force-sensing probe was assembled using an external-force-assisted nanorobotic assembly. Both the ES and EM forces were characterized quantitatively to show their contribution to the whole assembly process. The ES force is a relatively stronger force than the EM force in a SEM environment constraint. However, the hybrid approach of using both fields might be useful for a variety of future assembly tasks that will requires a certain amount of assembly force, such as, for example, soldering. The work is expected to be applied to real assembly tasks and steps toward future autonomous nanorobotic manufacturing. Table 11.4 summarizes the comparison of assembly steps in coarse and fine motions. The field-assist assembly reduces the assembly steps and improves the success rate and completion time.

Table 11.4 Summary of assembly process comparison: nanorobotic manipulation only and field assist

	NR only	Field assist
Coarse steps	9	6
Fine steps	9	4
Success rate	Rarely successful	Almost successful
Completion time	No limit	∼10 min

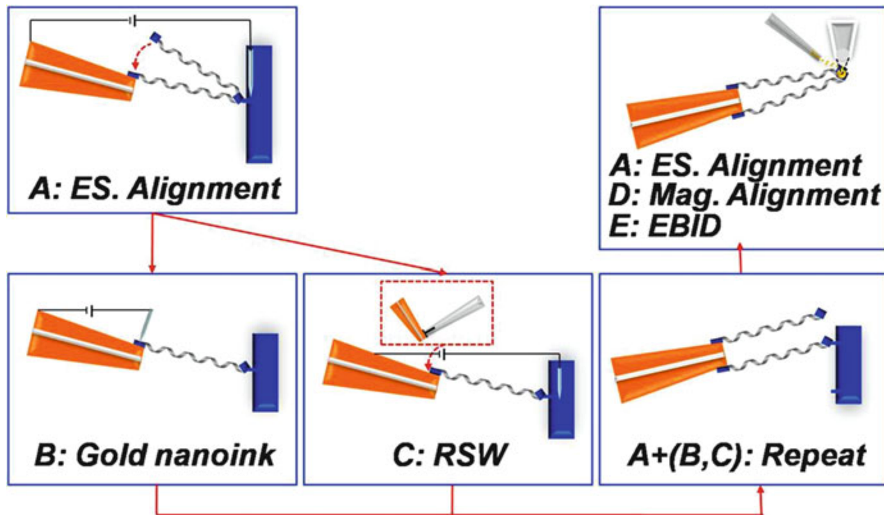

Fig. 11.8 Basic sensor assembly and calibration process sequence: (*A*) fabricated HNBs with metal connectors are aligned using electrostatic force on the two independently fabricated electrodes; (*B* and *C*) gold nanoink or RSW is used to solder the aligned HNBs for electrical measurement; (*D*) electromagnetic force is used to assist the assembly; (*E*) EBID is used to solder the aligned HNBs [[34] (©AIP 2012), reprinted with permission]

11.3.4 Force Sensor Assembly

Figures 11.8 and 11.9 depict the fabrication process. After the previous experiments, to test if the resistance spot welding (RSW) is an optimal choice to fix the HNB over the pipette, we concluded that this was the best way to create our final sensor prototype. In other words, RSW is a good choice because the generated contact is strong but is also a good conductor. After these observations, we decided to create a sensor using RSW. The procedure is similar to the previous one (assembly with glue and nanoink). This means that a pipette with double conductive layers, two picoprobes, chips with HNBs, and the necessary welding equipment was required. To create the sensor, first, HNBs were attached over the surface of the pipette. Figure 11.9 shows a coil attached over the pipette using RSW. As shown in Fig. 11.9, we broke the contact between the surface of the chip and the pad. When we were done with this side, we began with the other. The process was the same, and in the

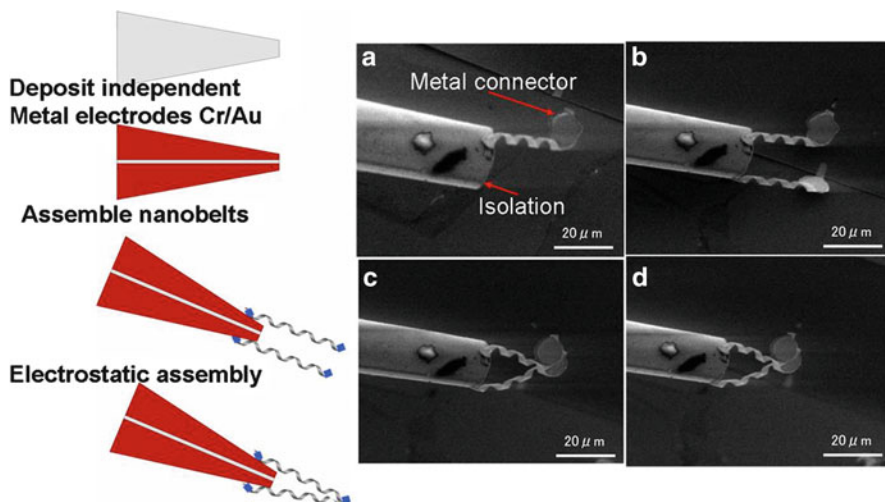

Fig. 11.9 Assembly procedure of HNBs on electrodes with pipette: (**a**) a side of an HNB is selected; (**b**) second HNB connection; (**c**) assembly by electrostatic force; (**d**) assembled device is moved [[34] (©AIP 2012), reprinted with permission]

end we obtained a device like that in the Fig. 11.9. To ensure contact, we decided to perform an extra process, electron-beam-induced deposition (EBID) (Fig. 11.9).

11.4 Characterizations

11.4.1 Giant Piezoresistivity of InGaAs/GaAs HNBs

For the electromechanical characterization experiments, two nanomanipulators (Kleindiek, MM3A), each with two metal probes (Picoprobe, T-4-10-1 mm) with a tip radius of 100 nm attached, were installed inside an SEM (Zeiss, DSM 962). The experimental procedure was explained in [35]. One manipulator was used to break and pick up a HNB on one side. For this purpose the HNBs were fabricated with a small length between the support and the first metal pad. The other manipulator was used to make contact with the other side. To achieve good electrical contacts on both sides of the HNBs, EBID with $W(CO)6$ precursor was used. In this way, a voltage could be applied to both sides of the HNBs and the current could be measured with a low-current electrometer (Keithley 6517A). After a HNB was attached as described, a tensile force was applied to it by moving one probe away from the other in the axial direction. Continuous frames of images were taken to analyze the deformation, and $I-V$ curves were recorded for the different positions. The characterization was carried out for three different HNBs. It was verified from

Table 11.5 Piezoresistivity and fabrication methods [21, 26, 35]

	Piezo. coef. $\pi_l^\sigma [10^{-10}\,\mathrm{Pa}^{-1}]$	Fabrication
Si bulk	1.7–9.4	MEMS
Bn-Si	4	MEMS
SiNW	3.5–355	Self-assembly
CNT	400	Self-assembly
HNB	996–3,560	Robotic assembly

the images that the boundary conditions did not change significantly during the experiments. The SEM images were analyzed to extract the HNB deformation for a certain $I-V$ measurement. This negative piezoresistivity behavior was observed in many different experiments and used as the force transduction of the proposed force sensors. The piezoresistivity of the structures can further be increased if Al is incorporated in the bilayer. Further details on the piezoresistive HNBs can be found in [35].

The material property of piezoresistivity in several piezoresistors is compared. The piezoresistance coefficients (π_l^σ) and fabrication methods of several piezoresistors are summarized in Table 11.5. The piezoresistance coefficients of HNBs were measured from our work (35). And Bn Si show that $|\pi_l^\sigma|$ is less than 10 $[10^{-10}\,\mathrm{Pa}^{-1}]$ [26]. But their fabrication was controlled with MEMS-compatible processes. It was recently reported that very large piezore- sistivities in SiNW and CNTs showed that a piezoresistance coefficient of $|\pi_l^\sigma|$ is 3.5–400 $[10^{-10}\,\mathrm{Pa}^{-1}]$ [21]. The high response was explained by the size effect. From this work, HNBs were found to be much higher ($|\pi_l^\sigma|$ was 996–3,560 $[10^{-10}\,\mathrm{Pa}^{-1}]$ [35]) than other piezoresistors. They are considered to be 249–890 times higher than Si piezoresistors. Therefore, HNBs are promising piezoresistors that will prove useful in high-resolution force sensors.

11.4.2 Force Transduction of Assembled HNB Force Sensor

The second experiment was conducted to characterize the assembled HNB force sensor. We aimed to measure the change in resistance when a force was applied and we wanted to find the parameters of the HNB for the force calibration. As we characterized the piezoresistive HNB, we expected to observe a change in resistance when a force was applied to it. Before we started this force transduction experiment, we needed to calibrate an AFM cantilever. For the mechanical characterization experiments, a nanomanipulator (Kleindiek, MM3A) and an AFM cantilever (Mikromasch, CSC38/Al BS, nominal stiffness 0.03 N/m) were installed inside the SEM (Zeiss, DSM 962). The AFM cantilever was calibrated using the method shown by Sader et al. [36], and the stiffness was found to be 0.132 N/m. Table 11.6 shows the proprieties of the cantilever and data items such as stiffness after calibration. The calibration procedure is shown in Fig. 11.10. The sensor pressed against the top of the cantilever, and so we measured the deflection of the

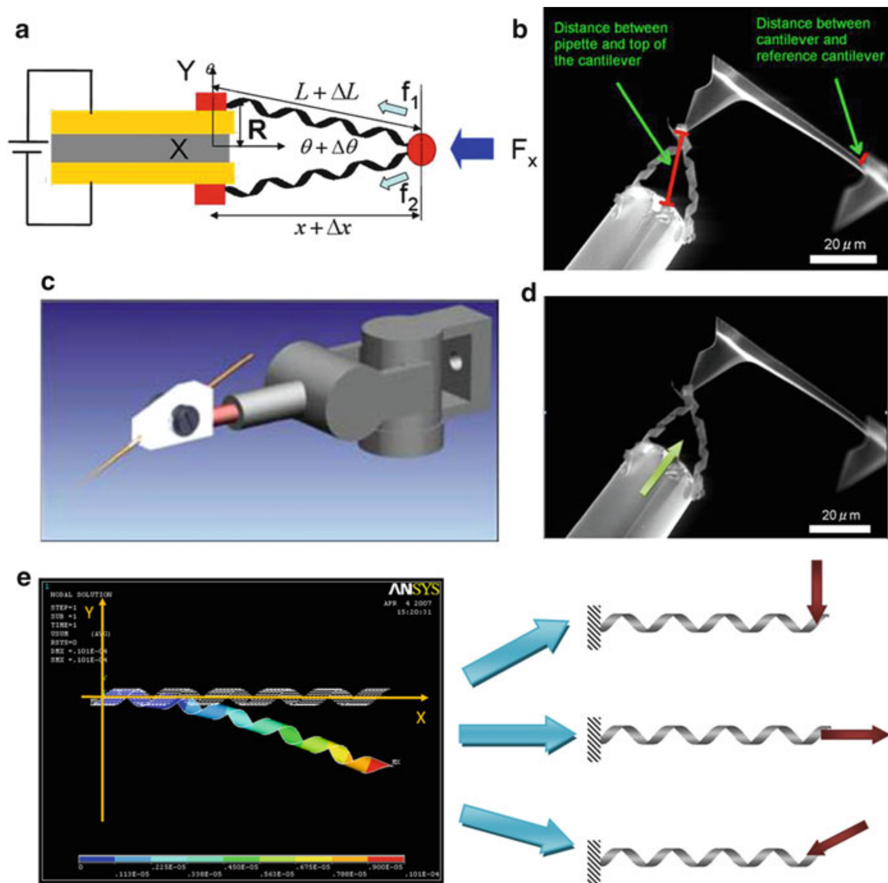

Fig. 11.10 Force measurement setup: (**a**) sensor geometry and force diagram; (**b**) SEM photo of calibration with AFM cantilever; (**c**) sensor mounted on manipulator; (**d**) SEM photo calibration after application of compressive force; (**e**) ANSYS simulation of HNB [[34] (©AIP 2012), reprinted with permission]

cantilever and the compression of the sensor. During these measurements, the data of the resistance change were saved. The process was as follows.

1. We took an initial picture of the experiment, made a voltage sweep from 0 to 1 [V], for a step of 0.1 [V], and recorded the measured current I [A] at each step. It was also important to measure the distance between the pipette and the top of the cantilever (for the compression of the sensor) and the distance between the cantilever used and the reference cantilever (see Fig. 11.10 for the deflection of the cantilever).
2. The pipette was moved forward. The sensor began to compress itself, and the cantilever started to deflect. As before, we swept the voltage from 0 to 1 [V] and measured the current I [A], and so we needed new photo frames for the calculation of the distances.

Table 11.6 Specification of cantilevers

Cantilever properties:	
Type	B
Length	350 ± 5 [µm]
Width	± 3 [µm]
Thickness	min = 0.7, typical = 1, max = 1.3 [µm]
Resonant frequency	min = 7, typical = 10, max = 14 [kHz]
Force constant	min = 0.01, typical = 0.03, max = 0.08 [N/m]
Cantilever after calibration:	
Stiffness	$K = 0.132$ [N/m]
Q-factor	$Q = 59.9$
Fluid density	1.18 [kg/m^3]
Fluid viscosity	1.86×10^{-5} [kg·m/s]

3. The last step was repeated for a few more cycles. After this procedure was finished, we needed to calculate the amount of force applied by the sensor against the cantilever. To calculate this, we needed to measure the deflection of the cantilever between the cantilever itself (touched) and the other cantilever (reference, Fig. 11.10). To calculate the force, we used Hooke's law ($F = k \cdot x$), where k is the stiffness of the cantilever. Now we knew the force for each compression of the sensor. The next step was to determine whether there was a relationship between the force and the change in resistance of the sensor. The resistance was calculated using Ohm's law at a constant voltage (1 V).

Measurement results are summarized in Figs. 11.11 and 11.12. We applied 0–80 nN in five different steps (trial 1) and applied 0–154 nN in a wider force range (trial 2) in Fig. 11.11. Better curves were observed in the second trial. In a smaller force range, deflection should be measured more carefully. SEM image frames were grabbed by the image acquisition software (DISS-5, Point Electronic GmbH) and analyzed using image processing software (DIPS, Point Electronic) to examine the cantilever deflections. The image analysis resolution of SEM was 100 nm, which could have minimum detectable forces of cantilever and HNB force sensing resolution of 13.2 nN and 2.42 nN respectively. The resistance changed at the second and third points of trial 1 while the same force was measured but the same 13.2 nN was recorded as in Fig. 11.12. Both trials show quite good repeatability. To further estimate the piezoresistivity behavior of HNBs, we decided to analyze HNB deflections that had much lower stiffness than that of the AFM cantilever. However, we needed to make the model estimate the force that could be eligible for experimental data. In the FEM simulation (axial direction) using ANSYS, we estimated a single HNB's axial stiffness as 0.0121 N/m. As the sensor had two angled HNBs connected at the end, a simple model to estimate stiffness of parallel aligned HNBs caused considerable error. In particular, the stiffness of the sensor varied by the angle change between the two HNBs when a force was applied. Finally, we wanted to determine the relation between the axial force on the sensor and the single HNB in the arm. Based on the geometric information from Fig. 11.10,

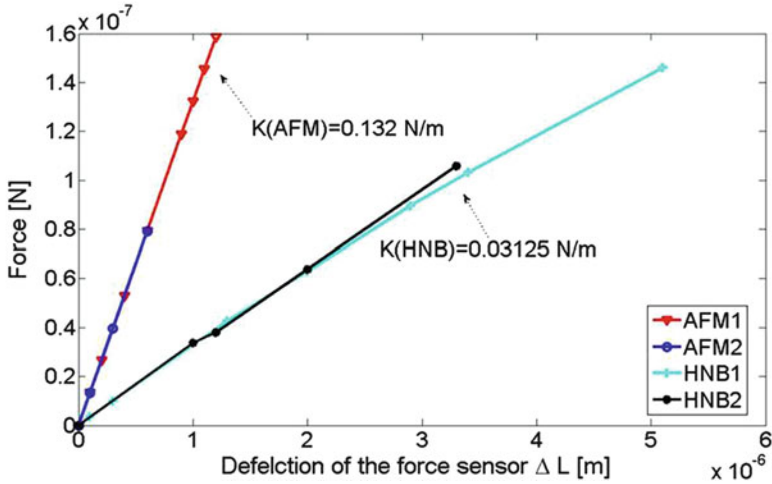

Fig. 11.11 Stiffness calibration of HNB force sensor using as-calibrated AFM cantilever [[34] (©AIP 2012), reprinted with permission]

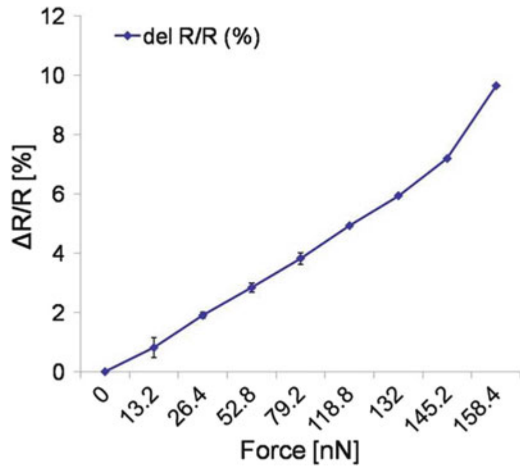

Fig. 11.12 Electromechanical measurements on a piezoresistive HNB force sensor: change in percentage of resistance as a function of axial force [nN] [[34] (©AIP 2012), reprinted with permission]

a trigonometric method was used to derive (11.2), which describes the mentioned relation. A detailed derivation is not included here:

$$K = \frac{2k_1 \Delta L}{\Delta X} \cos \frac{\theta}{2}. \tag{11.2}$$

where K is the stiffness of the sensor, k_1 is the stiffness of a single HNB, ΔX is the deflection of a single HNB arm, ΔL is the axial deflection of the sensor, and θ is the angle between two HNB arms. As the stiffness varied while the sensor underwent deflection, the model simulation of a sensor with constant stiffness

resulted in a nonuniform error during deflection. Therefore applying (11.2) to estimate the stiffness at each deflection yielded a better fitted calibration curve of the sensor model and real experiment, as shown in Fig. 11.11. It shows the stiffness difference between the AFM cantilever and the sensor, which varied by the deflection. Figure 11.11 shows the stiffness calibration of the HNB force sensor using an as-calibrated AFM cantilever. From the measurement, the stiffness of the HNB force sensor varied slightly by the deflection but was almost constant in the measured region. The stiffness of the measured HNB force sensor was approximately 0.03125 [N/m] compared with the value (0.132 [N/m]) of the as-calibrated AFM cantilever. Furthermore, the optimized design of the HNB force sensor could be predicted. From (11.2), the higher range of the force sensor could be designed by decreasing the angle (θ) and increasing the given design of individual HNBs. In addition to the assembly design parameters, the individual HNBs could also be tuned their stiffness. When the two HNBs are assembled serially (θ is 180°), the highest resolution but minimum range force sensing is possible. For a wider range of force sensing compensating for resolution, two HNBs should be assembled in parallel (θ is 180°).

Figure 11.12 shows the response of the piezoresistive HNB force sensor. The stiffness of HNB force sensor is close to the stiffness of the cantilever. It should be noted that these results are considered for an ideal simulation, where the device is symmetric and the HNBs have the same properties. The piezoresistance coefficient (π_l^σ) of the assembled sensor was calculated to be $515 \cdot 10^{-10}\,[\text{Pa}^{-1}]$ from the measurement and from (11.3):

$$\pi_l^\sigma = \frac{1}{X}\frac{\Delta\sigma}{\sigma_0}, \tag{11.3}$$

where σ_0 is the conductivity under zero stress and X is the stress applied. This is close to the individual HNB that was measured in a range of 996–3,560$\cdot 10^{-10}$ [Pa^{-1}]. It should be noted that the stiffness of the assembled structure was almost doubled; thus the piezoresistance coefficient was decreased by half. It could explain the fact that the design of triangular shape of the HNB force sensor did not sacrifice the force sensitivity compared to the single HNB. The stiffness of the HNB force sensors can also be tuned by the assembly geometry using constant stiffness of individual HNBs. It allows for the control of the force-sensing range and resolution by editing both the assembly and individual HNBs' design parameters. The calibration experiment and simulation based on the assembled force sensor model shown here were not ideal for measuring the sensitivity of force sensing. It should be considered that the calibration was performed in a full force-sensing range to verify how the piezoresistivity of HNBs contributed to measuring the force in the range. To measure to more accurately measure the sensing resolution, we should apply smaller force steps (displacement) under magnified SEM image. Another consideration is on the shape of the sensor (Fig. 11.10). The minimum detectable force resolution using an individual HNB was estimated to be 0.91 nN by considering the standard deviation of the measured noise (0.03 nA), which is within the range of the high-resistance electrometer (Keithley 6517 A, measurable up to 1 fA).

11.5 Conclusions

Large bandwidth force sensing based on thin-film three-dimensional nanostructures could be a useful tool for various micro-/nanomanipulation applications. For example, this chapter described a manufacturing challenge and the proposed assembly process of thin-film piezoresistive HNB force sensors assembled by nanorobotic manipulations. The proposed process consists of assembly, characterizations, and calibrations done in an in situ manner inside a SEM. The assembled HNB force sensors showed a large displacement range, high-resolution force sensing, self-sensing, and low weight as a result of the unusually high piezoresistivity, low stiffness, and high-strain capability of HNBs. There are open applications from electronics (electric contact probing and testing for microelectronic circuits), biology (wide range mechanical characterizations of tissues, fibers), and MEMS/NEMS (mechanical characterizations of CNTs, NWs). Moreover, this alternative technology to the conventional micro-/nanomanufacturing process holds great potential for MEMS/NEMS.

Acknowledgements This work was sponsored by the Japan Society for the Promotion of Science (JSPS) research fellow program and the Ministry of Education, Science and Culture, Japan. I would like to thank Bradley J. Nelson, Dominik J. Bell, Lixin Dong, and Li Zhang at IRIS ETHZ for my research visit and valuable discussions.

References

1. R. Smith, D.R. Sparks, D. Riley, D. Najafi, A MEMS-based coriolis mass flow sensor for industrial applications. IEEE Trans. Ind. Electron. **56**(4), 1066–1071 (2009)
2. R. Saeidpourazar, N. Jalili, Microcantilever-based force tracking with applications to high-resolution imaging and nanomanipulation. IEEE Trans. Ind. Electron. **55**(11), 3935–3943 (2008)
3. H.J. Dai, J.H. Hafner, A.G. Rinzler, D.T. Colbert, R.E. Smalley, Nanotubes as nanoprobes in scanning probe microscopy. Nature **384**(6605), 147–150 (1996)
4. J.H. Hafner, C.L. Cheung, T.H. Oosterkamp, C.M. Lieber, High-yield assembly of individual single-walled carbon nanotube tips for scanning probe microscopies. J. Phys. Chem. B **105**(4), 743–746 (2001)
5. J. Li, A.M. Cassell, H.J. Dai, Carbon nanotubes as AFM tips: measuring DNA molecules at the liquid/solid interface. Surf. Int. Anal. **28**(1), 8–11 (1999)
6. S. Iijima, Helical microtubules of graphitic carbon. Nature **354**, 56–58 (1991)
7. Y. Cui, C.M. Lieber, Functional nanoscale electronic devices assembled using silicon nanowire building blocks. Science **291**(5505), 851–853 (2001)
8. S. Motojima, M. Kawaguchi, K. Nozaki, H. Iwanaga, Growth of regularly coiled carbon filaments by Ni catalyzed pyrolysis of acetylene, and their morphology and extension characteristics. Appl. Phys. Lett. **56**(4), 321–323 (1990)
9. X.B. Zhang, X.F. Zhang, D. Bernaerts, G.T. Vantendeloo, S. Amelinckx, J. Vanlanduyt, V. Ivanov, J.B. Nagy, P. Lambin, A.A. Lucas, The texture of catalytically grown coil-shaped carbon nanotubules. Europhys. Lett. **27**(2), 141–146 (1994)
10. X.Y. Kong, Z.L. Wang, Spontaneous polarization-induced nanohelixes, nanosprings, and nanorings of piezoelectric nanobelts. Nano Lett. **3**(12), 1625–1631 (2003)

11. P.X. Gao, Y. Ding, W.J. Mai, W.L. Hughes, C.S. Lao, Z.L. Wang, Conversion of zinc oxide nanobelts into superlattice-structured nanohelices. Science **309**(5741), 1700–1704 (2005)
12. D.J. Bell, Y. Sun, L. Zhang, L.X. Dong, B.J. Nelson, D. Grutzmacher, Three-dimensional nanosprings for electromechanical sensors. Sens. Act. A-Phys. **130**, 54–61 (2006)
13. D.J. Bell, L.X. Dong, B.J. Nelson, M. Golling, L. Zhang, D. Grutzmacher, Fabrication and characterization of three-dimensional InGaAs/GaAs nanosprings. Nano Lett. **6**(4), 725–729 (2006)
14. G. Yang, J.A. Gaines, B.J. Nelson, Optomechatronic design of microassembly systems for manufacturing hybrid microsystems. IEEE Trans. Ind. Electron. **52**(4), 1013–1023 (2005)
15. E. Enikov, L. Minkov, S. Clark, Microassembly experiments with transparent electrostatic gripper under optical and vision-based control. IEEE Trans. Ind. Electron. **52**(4), 1005–1012 (2005)
16. B. Borovic, A. Liu, D. Popa, H. Cai, F. Lewis, Light-intensity-feedback-waveform generator based on MEMS variable optical attenuator. IEEE Trans. Ind. Electron. **55**(1), 417–426 (2008)
17. J.J. Abbott, Z. Nagy, F. Beyeler, B.J. Nelson, Robotics in the small, part I: microrobotics. IEEE Rob. Auto. Mag. **14**(2), 92–103 (2007)
18. L.X. Dong, B.J. Nelson, Robotics in the small, part II: nanorobotics. IEEE Rob. Auto. Mag. **14**(3), 111–121 (2007)
19. D. Golberg, P. Costa, O. Lourie, M. Mitome, C. Tang, C. Zhi, K. Kurashima, Y. Bando, Direct force measurements and kinking under elastic deformation of individual multiwalled boron nitride nanotubes. Nano Lett. **7**(7), 2146–2151 (2007)
20. L. Zhang, L. Dong, B.J. Nelson, Bending and buckling of rolled-up SiGe/Si microtubes using nanorobotic manipulation. Appl. Phys. Lett. **92**, 243102 (2008)
21. C. Bustamante, Z. Bryant, S.B. Smith, Ten years of tension: single-molecule DNA mechanics. Nature **421**, 423–427 (2003)
22. C. Bustamante, J.C. Macosko, G.J.L. Wuite, Grabbing the cat by the tail: manipulating molecules one by one. Nature Rev. Mol. Cell. Biol. **1**, 130–136 (2000)
23. A. Kishino, T. Yanagida, Force measurements by micromanipulation of a single actin filament by glass needles. Nature **334**, 74–76 (1988)
24. A. Ashkin, J.M. Dziedzic, Optical trapping and manipulation of viruses and bacteria. Science **235**(4975), 1517–1520 (1987)
25. S.B. Smith, L. Finzi, C. Bustamante, Direct mechanical measurements of the elasticity of single DNA-molecules by using magnetic beads. Science **258**(5085), 1122–1126 (1992)
26. C. Stampfer, T. Helbling, D. Obergfell, B. Schoberle, M.K. Tripp, A. Jungen, S. Roth, V.M. Bright, C. Hierold, Fabrication of single-walled carbon-nanotube-based pressure sensors. Nano Lett. **6**(2), 233–237 (2006)
27. C. Stampfer, A. Jungen, R. Linderman, D. Obergfell, S. Roth, C. Hierold, Nano-electromechanical displacement sensing based on single-walled carbon nanotubes. Nano Lett. **6**, 1449–1453 (2006)
28. T.C. Duc, J.F. Creemer, P.M. Sarro, Lateral nano-Newton force-sensing piezoresistive cantilever for microparticle handling. J. Micromech. Microeng. **16**(6), S102–S106 (2006)
29. B.L. Pruitt, W.T. Park, T.W. Kenny, Measurement system for low force and small displacement contacts. J. Microelectromech. Syst. **13**(2), 220–229 (2004)
30. F. Beyeler, A. Neild, S. Oberti, D.J. Bell, Y. Sun, J. Dual, B.J. Nelson, Monolithically fabricated micro-gripper with integrated force sensor for manipulating micro-objects and biological cells aligned in an ultrasonic field. J. Microelectromech. Syst. **16**(1), 7–15 (2007)
31. L. X. Dong, L. Zhang, D.J. Bell, B.J. Nelson, D. Grutzmacher, Hybrid nanorobotic approaches for fabricating NEMS from 3D helical nanostructures. Proc. IEEE ICRA, Orlando, Florida, U.S.A., 1396–1401 (2006)
32. G. Hwang, C. Dockendorf, D.J. Bell, L.X. Dong, H. Hashimoto, D. Poulikakos, B.J. Nelson, 3-D InGaAs/GaAs helical nanobelts for optoelectronic devices. Int. J. Optomech. **2**, 88–103 (2008)
33. P. Kim, C.M. Lieber, Nanotube nanotweezers. Science **286**, 2148–2150 (1999)
34. G. Hwang, H. Hashimoto, Helical nanobelt force sensors. AIP Rev. Sci. Inst. **83**, 126102 (2012)

35. G. Hwang, H. Hashimoto, D.J. Bell, L.X. Dong, B.J. Nelson, S. Schon, Piezoresistive InGaAs/GaAs nanosprings with metal connectors. Nano Lett. **9**(2), 554–561 (2009)
36. J.E. Sader, J.W.M. Chon, P. Mulvaney, Calibration of rectangular atomic force microscope cantilevers. AIP Rev. Sci. Inst. **70**, 3967–3969 (1999)